

A reprint from

OPTICAL ENGINEERING

July 1996

ISSN 0091-3286

INTEGRATED OPTICAL SIGMA-DELTA MODULATORS

Phillip E. Pace
Stephen J. Ying
John P. Powers
Ronald J. Pieper

Integrated optical sigma-delta modulators

Phillip E. Pace, MEMBER SPIE

Stephen J. Ying

John P. Powers, MEMBER SPIE

Ronald J. Pieper, MEMBER SPIE

Naval Postgraduate School

Department of Electrical and Computer
Engineering

Code EC/PC

Monterey, California 93943

E-mail: pace@pcpep.ece.nps.navy.mil

Abstract. Modern avionics equipment, such as superresolution direction-finding systems (frequency band 0.3 to 3 MHz), now require resolutions greater than 15 bits. Oversampled analog-to-digital converter architectures offer a means of exchanging resolution in time for that in amplitude and represent an attractive approach to implementing precision converters without the need for complex precision analog circuits. Using oversampling techniques based on sigma-delta ($\Sigma\Delta$) modulation, a convenient trade-off exists between sampling rate and resolution. One of the major advantages of integrated optics is the capability to efficiently couple wideband signals into the optical domain. Typically, $\Sigma\Delta$ processors require simple and relatively low precision analog components and thus are well suited to integrated optical implementations. The current $\Sigma\Delta$ methodology is reviewed and the design of the single-bit, integrated optical $\Sigma\Delta$ modulator is presented. Simulation results for both first- and second-order architectures are presented by evaluating the transfer characteristics numerically. A 16-bit $f_0=1$ MHz design (oversampling ratio of 132) is also quantified. © 1996 Society of Photo-Optical Instrumentation Engineers.

Subject terms: optical analog-to-digital converters; sigma-delta; direction finding systems.

Paper 15085 received Aug. 14, 1995; revised manuscript received Dec. 2, 1995; accepted for publication Dec. 3, 1995.

1 Introduction

Analog-to-digital converters (ADCs) are basic building blocks for a wide variety of digital systems. A partial list of ADC applications includes process control, automatic test equipment, video signal acquisition, audio recordings for compact discs, and interfaces for personal computers. There exists a variety of approaches to the ADC design. One approach, known as delta modulation, involves the use of oversampling methods. First introduced in the 1940s, delta modulation uses oversampling and single-bit code words to represent the analog signals.¹ The simplest approach counted the output bits from the delta modulator with a high bit representing $a+1$ and a low bit representing $a-1$. The output was then resampled at the Nyquist rate. Resolution proved to be a problem, since achieving adequate reproduction of speech signals required oversampling ratios of the order 5000. More effective digital filtering was needed to prevent the high-frequency modulation noise from aliasing into the signal band when it was resampled at the Nyquist rate.

Unfortunately at that time, digital filters used for this purpose were prohibitively expensive. Candy proposed an interpolative technique for digital filtering.² The idea was to digitize the signal through the use of a coarse quantizer and cause the output to oscillate between the quantized levels at high speed so that its average value over the Nyquist interval was an accurate representation of the sampled value. The digital filters used to generate this average were inexpensive. On the other hand, these digital filters also proved to be reliable and fairly tolerant of circuit imperfections. The quantizers for these interpolating converters utilized a noise-shaping technique that measures the quantization er-

ror in one sample and subtracts it from the next input sample value.³ The most popular form of this noise-shaping technique is known as sigma-delta ($\Sigma\Delta$) modulation. Sigma delta modulators employ integration and feedback in iterative loops to obtain high-resolution analog-to-digital (A/D) conversions.

Specifically, a sigma-delta modulator ($\Sigma\Delta M$) consists of an analog filter and a quantizer enclosed in a feedback loop.⁴ Together with the filter, the feedback loop acts to attenuate the quantization noise at low frequencies while amplifying the high-frequency noise. Since the signal is oversampled at many times the Nyquist rate, a digital low-pass filter can be used to remove the high-frequency quantization/modulation noise without affecting the signal band. This filtering usually involves a multistage decimation process since the output of the modulator represents the signal with the high-frequency modulation noise as well as its out-of-band components, which dominate at the lower frequencies. In general, the smoothing characteristics involved in the decimation process require that the signal propagate through several filters and resampling stages. The first stage of decimation lowers the word rate to an intermediate frequency, where a filter removes the high-frequency modulation noise. A second low-pass filter is then used to attenuate the out-of-band components before the signal is resampled at its Nyquist rate. As the signal propagates through the filters and resampling stages, the word length increases to preserve the resolution. A more thorough discussion of multistage decimation and filtering can be found in Ref. 1.

The transmission of coherent light through optical waveguides has been of great interest ever since the late

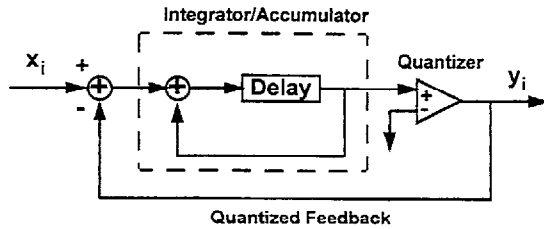


Fig. 1 Block diagram of a first-order all-electronic $\Sigma\Delta M$.

1960s. Through this interest emerged the concept of integrated optics, in which wires and radio links are replaced by light-waveguiding optical fibers and conventional electrical integrated circuits are replaced by miniaturized optical integrated circuits (OICs). Optical components offer a number of advantages over their electronic counterparts. These advantages include large bandwidth, use of optical sources capable of high-speed switching [which is necessary for high pulse repetition frequencies (PRFs)], low power consumption, improved reliability, and insensitivity to vibration and electromagnetic interference (EMI). A key advantage is the increased characteristic bandwidth over electronic components. The carrier medium is a lightwave rather than an electrical current. Thus the frequency limiting effects of capacitance and inductance can be avoided. Since electronic converters based on $\Sigma\Delta$ modulation require oversampling, their applicability is mainly limited to low and moderate signal frequencies. The use of optical integrated components provides an attractive solution to the otherwise bandlimited electronic $\Sigma\Delta$ architecture. Previous researchers have investigated the use of multiple-quantum-well self-electro-optic effect devices within a bulk-optic error diffusion architecture.⁵ A first-order modulator was demonstrated⁶ at a sampling frequency of 1 kHz. The extension to a second-order architecture was proposed in Ref. 7. Vibration, thermal instabilities, atmospheric turbulence, and scattering can, however, impose severe problems for these types of free-space processors, eliminating their use on platforms that are mobile or airborne.

This paper describes a single-bit, integrated optical $\Sigma\Delta M$ approach. In Sec. 2, the all-electronic $\Sigma\Delta$ modulator is reviewed. Both first- and second-order architectures are discussed. Analysis and simulation results for both the first- and second-order models are presented. In Sec. 3, an integrated optical architecture for a first- and second-order $\Sigma\Delta$ modulator is introduced. The optical devices used for implementation are explained and compared at a component level to the all-electronic design. Simulation results are presented and analyzed. In Sec. 4, the relationship between oversampling and resolution is detailed and discussed in terms of the modulator SNR. In Sec. 5, a 16-bit, $f_0=1$ MHz design (oversampling ratio=132) is described in detail. Finally, issues concerning the current simulation model and future efforts are discussed.

2 All-Electronic, Single-Bit $\Sigma\Delta$ Modulators

2.1 First-Order $\Sigma\Delta M$

A sampled-data equivalent of a first-order $\Sigma\Delta M$ is shown in Fig. 1. Because this is a sampled-data circuit, the inte-

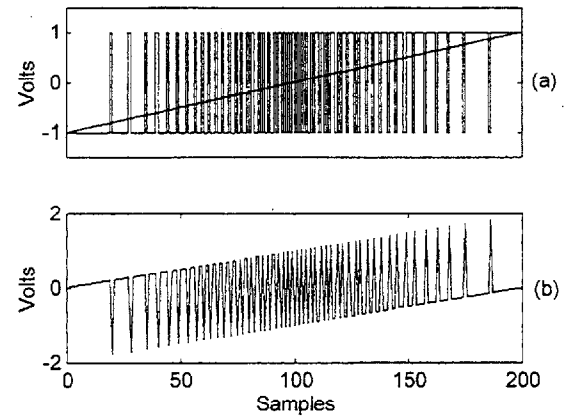


Fig. 2 First-order all-electronic $\Sigma\Delta M$: (a) comparator output and sampled input and (b) output of accumulator stage.

gration is performed via an accumulator. The analog signal is assumed to be oversampled at well above the Nyquist frequency. This sampled input x_i is fed to the quantizer via the accumulator. The quantized output, which can be modeled as an approximation of the quantization error, is fed back and subtracted from the input. This quantized, feedback signal forces the average value of the quantized output y_i to track the average value of the input signal. Any difference accumulates in the integrator and eventually corrects itself.

The quantization error is subtracted from the input value and the difference becomes the input for the next cycle. After the process is repeated many times at high speed, an average of the digital outputs occurring in each sample time becomes a useful digital representation of the input signal. In a stable converter, the oscillations of the quantized value are bounded, that is, it has a limit cycle. In general, this quantization process can be performed over more than one quantization level.¹ By this process, it can be seen that the speed of operation obviates the need for precise circuit elements. Precision in the quantization levels of the quantizer is not a stringent requirement since the average of the quantized output y_i will automatically be adjusted to agree with the sampled input analog signal x_i . Therefore the output of the $\Sigma\Delta$ modulation process can provide a high level of precision in the representation despite coarseness in the quantization levels.

The input/output transfer characteristics of the first-order $\Sigma\Delta M$ are plotted in Fig. 2(a). The signal oscillates between the quantized levels in such a manner that its local average equals the average input. For this example the input signal is ramped with 200 samples with a ± 1 V range. The comparator output voltage is ± 1 V with the threshold voltage set at 0 V. Figure 2(b) shows the limit cycles at the output of the accumulator. These simulation results are in agreement with previously reported predictions for first-order $\Sigma\Delta$ modulators.¹

2.2 Second-Order $\Sigma\Delta M$

Although the first-order model is the simplest, the quantization noise is highly correlated to the input, resulting in excessive limit cycles. Extending the architecture to a

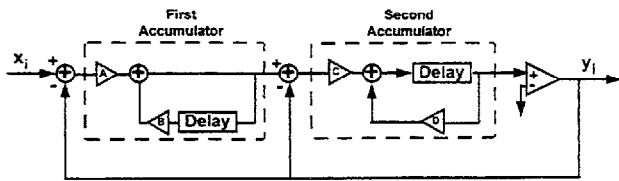


Fig. 3 Block diagram of a second-order all-electronic $\Sigma\Delta M$.

second-order modulator eliminates a number of instabilities and increases the reliability of the circuit. However, higher order designs (greater than 2) suffer from instability due to the undesirable limit cycles (bounded oscillations) which result in the accumulation of large signals in the integrators.⁴

A sampled-data equivalent circuit diagram of a second-order electronic $\Sigma\Delta M$ is shown in Fig. 3. The first accumulator, which embeds the delay in the feed-backward path, has a transfer function given by

$$H_1(z) = \frac{A}{1 - Bz^{-1}}, \quad (1)$$

where the coefficients A and B are the gains of the system. The second accumulator stage embeds the delay in the feed-forward path. Its transfer function is given by

$$H_2(z) = \frac{Cz^{-1}}{1 - Dz^{-1}}, \quad (2)$$

where coefficients C and D are the loop system gains. For this example all coefficient values are ideally set at unity. As in the first order $\Sigma\Delta M$, the comparator output voltage is ± 1 volt with the threshold voltage set at zero volts.

The response of the second-order $\Sigma\Delta M$ is illustrated in Fig. 4. The input used for simulation consists of 200 data samples ramped from -1 V to $+1$ V in increments of 0.01 V. The duty cycles of the quantizer output are weighted toward the average value of the input. That is, at the start of the ramped input the duty cycles are weighted toward the bottom-level quantization [Fig. 4(a)]. Toward the center of the input, the duty cycles are at about 50%. At the high end of the ramp, they are weighted toward the top-level quantization. Figure 4(b) shows the signal value at the output of the accumulator stages. From the output of accumulator 1, it can be easily seen that the output is oscillating about the ramped input range of -1 to $+1$ V. Results of the second-order modulator illustrate how a second feedback loop attenuates the excessive limit cycles (due to high correlation of the quantization noise) found in the first-order modulator.¹

Although not part of the current modulator investigation, a decimation filter can then be used to resample the quantized signal at the Nyquist rate. This serves to eliminate any out-of-band quantization noise. It also determines the ratio of the sampled, quantized outputs over the Nyquist interval. This average value proves to be highly representative of the input value.

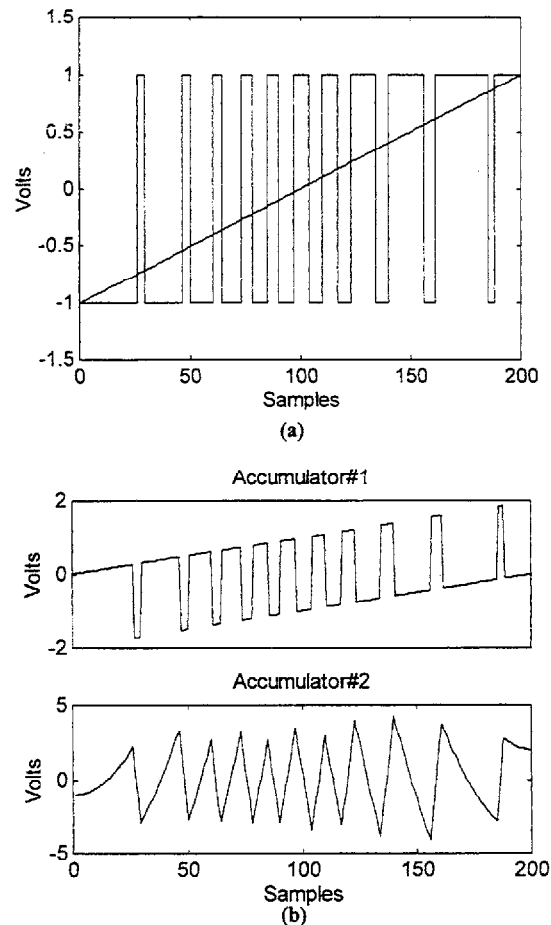


Fig. 4 Second-order all-electronic $\Sigma\Delta M$: (a) comparator output and sampled input and (b) input at first and second accumulator stages.

3 Integrated-Optical, Single-Bit $\Sigma\Delta$ Modulators

3.1 First-Order $\Sigma\Delta M$

A block diagram of a first-order integrated optical $\Sigma\Delta M$ is shown in Fig. 5. In applying optical integrated components to a $\Sigma\Delta$ architecture, a first-order model is first simulated. In the integrated optical design, laser pulses from a mode-locked laser are used to oversample the rf signal. To gain a better understanding of the model, the integrated optical components used are described in detail.

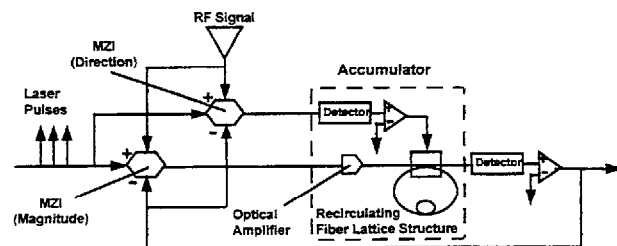


Fig. 5 Block diagram of a first-order integrated optical $\Sigma\Delta M$.

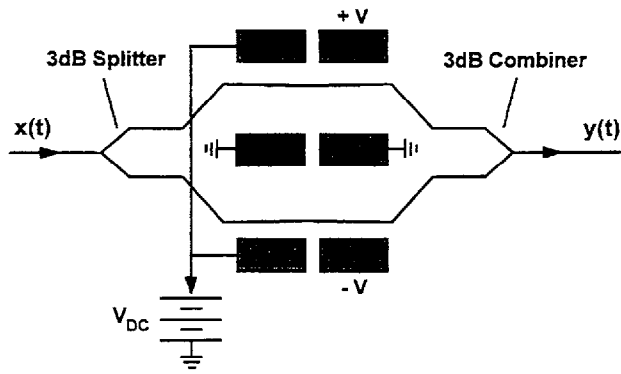


Fig. 6 Schematic diagram of an MZI in a push-pull configuration.

3.1.1 Mach-Zehnder interferometer

The Mach-Zehnder interferometer (MZI) is used to efficiently couple the wideband rf signal into the optical domain. It also serves to subtract the feedback signal from the input signal. Figure 6 shows a schematic diagram of an MZI. The input pulse is split into equal components, each of which propagates over one arm of the interferometer. The optical paths of the two arms are equal. If no phase shift is introduced between the interferometer arms, the two components combine in phase at the output and continue to propagate undiminished. For the current design, a three-electrode configuration is used to achieve a push-pull phase change.⁸ The push-pull effect increases the phase change efficiency of the device. This configuration is utilized to subtract the feedback signal from the next input value. To take advantage of this push-pull configuration, the feedback voltage polarity from the comparator must be reversed. The transfer function of the MZI can be expressed⁹ as

$$I_{out} = I_{in} \left\{ \frac{1}{2} + \frac{1}{2} \cos[\Delta\phi(\nu) + \theta] \right\} \quad (3)$$

where

$$\Delta\phi(\nu) = \frac{2\pi n_e^3 r \Gamma L_i \nu}{G\lambda} \quad (4)$$

is the voltage-dependent phase shift and is a function of the effective index of the optical guide n_e , the pertinent electro-optic coefficient r , the interelectrode gap G , the electrical-optical overlap parameter Γ , and the free-space optical wavelength λ . The modulation voltage, $\nu = V_{FF} - V_{FB}$, serves to subtract the feedback signal from the next input value.

The method of accumulation involves the magnitude of the signal to be accumulated and the direction of accumulation. In the case of the first-order $\Sigma\Delta M$, two interferometers are used for the accumulator stage. One interferometer provides the magnitude for the accumulator. The other interferometer is used to determine the direction of accumulation. Figure 7 plots the transfer functions for both interferometers. Both MZIs map the input signal to an output intensity between 0 and 1 (light intensity cannot be negative). The transfer functions are the same except for the dc bias θ , which is added to the phase shift. For the MZI

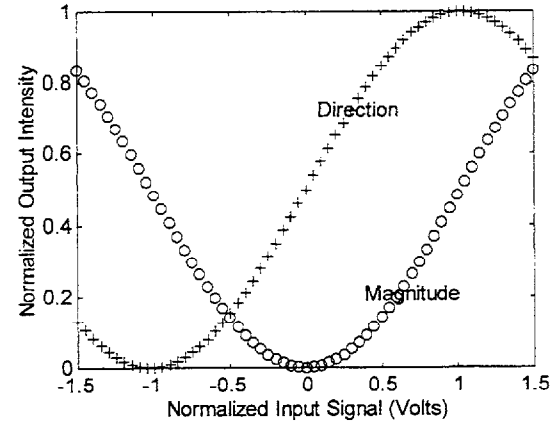


Fig. 7 Transfer characteristic of the MZI.

controlling the magnitude of the signal, $\theta = \pi$. The MZI controlling the direction of accumulation has $\theta = -\pi/2$.

From the transfer functions, the output values for magnitude range from 0 to 0.5 and are symmetric about the input value of zero. The output values for the direction range from 0 to 1. The accumulator comparator threshold voltage is normalized at 0.5 volts. The detected direction intensity from the MZI is compared to the normalized threshold to determine whether the intensity from the magnitude MZI accumulates upward or downward. The recirculating fiber lattice structure accumulates downward if the output of the interferometer is less than 0.5 and upward for values greater than 0.5. Thus the detector, comparator and optical recirculator serve to function as an accumulator.

3.1.2 Fiber lattice structures

Fiber optic lattice structures incorporating single-mode fibers and directional couplers are used to instrument the accumulators. These fiber structures can be used to perform various frequency-domain functions such as matrix operations and frequency filtering.¹⁰ Two structures basic to fiber signal processing include the two-coupler nonrecirculating and the two-coupler recirculating delay lines. For design of the optical $\Sigma\Delta$ modulator, a recirculating feed-backward fiber lattice structure is utilized for the accumulator. The generalized form of a two-coupler, 4-port recirculating fiber delay line is shown in Fig. 8. Moslehi et al.¹⁰ described the

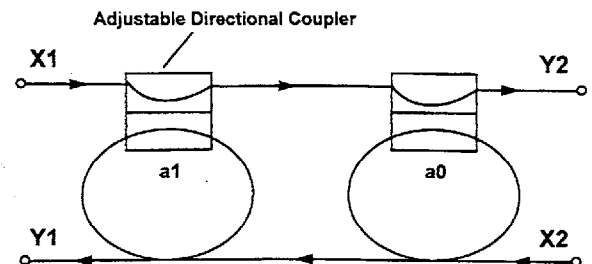


Fig. 8 Block diagram of a recirculating fiber optic lattice structure.

z -transform transfer matrix of this recursive structure. The inputs and outputs are related to each other by

$$\begin{bmatrix} Y_1(z) \\ Y_2(z) \end{bmatrix} = \begin{bmatrix} H_{11}(z) & H_{12}(z) \\ H_{21}(z) & H_{22}(z) \end{bmatrix} \begin{bmatrix} X_1(z) \\ X_2(z) \end{bmatrix}. \quad (5)$$

The transfer functions within the transfer matrix are

$$H_{11}(z) = \frac{a_1 - (1 - 2a_1)a_0L_1z^{-1}}{1 - a_1a_0L_1z^{-1}}, \quad (6)$$

$$H_{21}(z) = \frac{1}{1 - a_0a_1L_1z^{-1}}, \quad (7)$$

$$H_{12}(z) = [(1 - 2a_0 - 2a_1 + 4a_0a_1 + a_0^2a_1^2 + a_0^2 - 2a_0^2a_1 + a_1^2 - 2a_1^2a_0)L_1z^{-1}] / (1 - a_0a_1L_1z^{-1}), \quad (8)$$

$$H_{22}(z) = \frac{-a_0 - a_1(1 - 2a_0)L_1z^{-1}}{1 - a_1a_0L_1z^{-1}}, \quad (9)$$

and describe the use of the general structure, where $H_{mn}(z)$ is the transfer function from input X_n to output Y_m . Thus $H_{21}(z)$ relates the X_1 input and Y_2 output and $H_{12}(z)$ relates the X_2 input and Y_1 output. The parameters a_0 and a_1 are the intensity coupling coefficients of the directional couplers and L_1 is the loop intensity transmittance of the system. For convenience, L_1 is assumed to be 1 (no losses in the system). The accumulator comparator voltage is then used to bias the directional coupler a_1 to create a phase change between the two pulses to perform the accumulation.

The accumulator stage in the first-order model has a transfer function given by Eq. (2). From the transfer matrix of the recirculating fiber lattice structure, $H_{12}(z)$ matches this form, where

$$C = 1 - 2a_0 - 2a_1 + 4a_0a_1 + a_0^2a_1^2 + a_0^2 - 2a_0^2a_1 + a_1^2 - 2a_1^2a_0 \quad (10)$$

and

$$D = a_0a_1 \quad (11)$$

are the corresponding gain values. The specific lattice configuration is shown in Fig. 9(b). The coupling coefficients a_0 and a_1 represent the percentage of light intensity coupled and therefore bounded between 0 and 1. The desired values for C and D would be unity. However, the two equations work against each other simultaneously as shown in Fig. 10. Here $a_0 = 0.3$ and a_1 varies from 0 to 1. Values near the intersection of C and D provide the best results ($a_1 = 0.5$, $C = 0.122$, $D = 0.15$). To compensate for the small value of C , an optical amplifier with a gain of 100 is placed just prior to the fiber lattice structure in the accumulator stage (see Fig. 5). Figure 11 plots the transfer characteristic of the first-order integrated optical $\Sigma\Delta M$. It is apparent that the first-order system is not stable enough for accurate conversion of the signal due to excessive limit cycles.

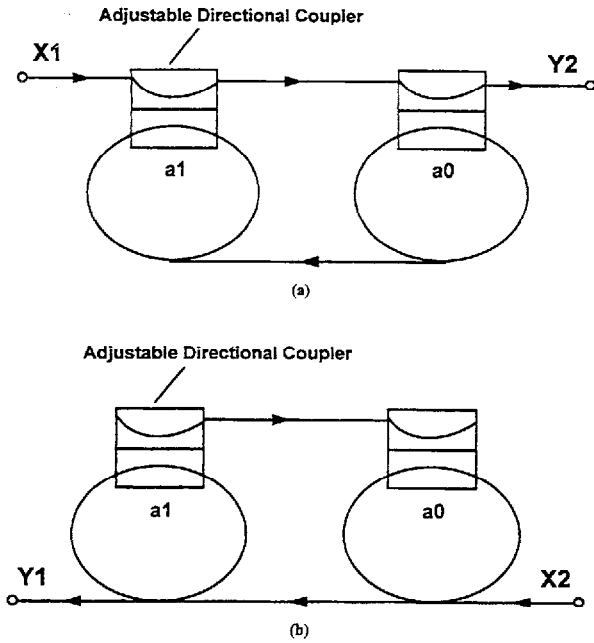


Fig. 9 Block diagrams of specific fiber lattice configurations used for electro-optic $\Sigma\Delta M$: (a) first accumulator stage with transfer function $H_{21}(z)$ and (b) second accumulator stage with transfer function $H_{12}(z)$.

3.2 Second-Order $\Sigma\Delta M$

The block diagram for a second-order integrated optical $\Sigma\Delta M$ is shown in Fig. 12. The specific fiber lattice structure configurations used for the two accumulator stages are shown in Fig. 9. The first stage (accumulator 1) has the transfer function described by Eq. (1) and uses $H_{21}(z)$ given by Eq. (7). The coupler coefficients are set ideally at unity, thus the gains A and B are also set at unity. The second stage (accumulator 2) is identical to the accumulator stage in the first-order $\Sigma\Delta M$. The coupler coefficients are again $a_0 = 0.3$ and $a_1 = 0.5$ and the gain of the optical amplifier is now 15.

Simulation results for the second-order integrated optical $\Sigma\Delta M$ are plotted in Fig. 13. The average value of the

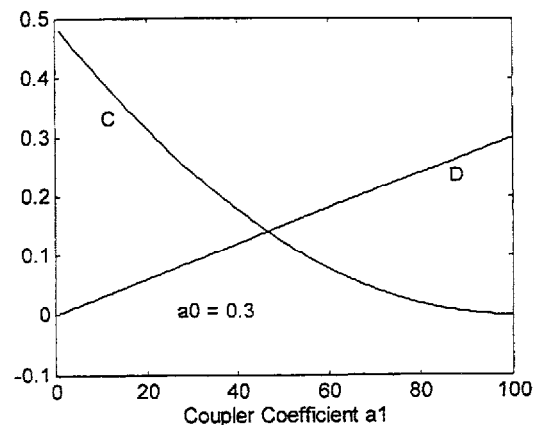
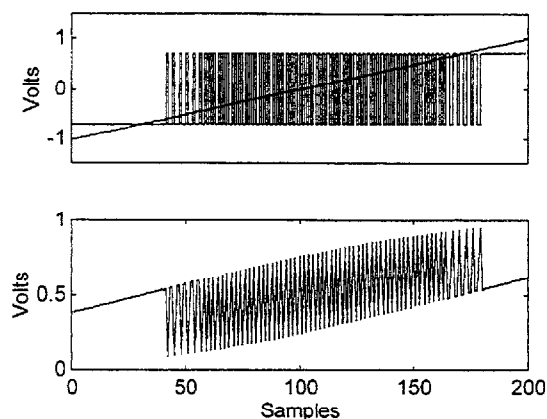


Fig. 10 Plot of accumulator gains C and D as functions of a_0 and a_1 .


 Fig. 11 Transfer characteristic of first-order electro-optic $\Sigma\Delta M$.

quantizer output can be seen to track the average value of the ramped input, as shown in Fig. 13(a). The output of the interferometer can be seen to oscillate about the ramped input. Figure 13(b) plots the intermediate signal values at the input of the MZIs in the accumulator stages. These results compare favorably to those of the all-electronic design and demonstrate the feasibility of the integrated optical approach.

4 Oversampling Ratio and Resolution

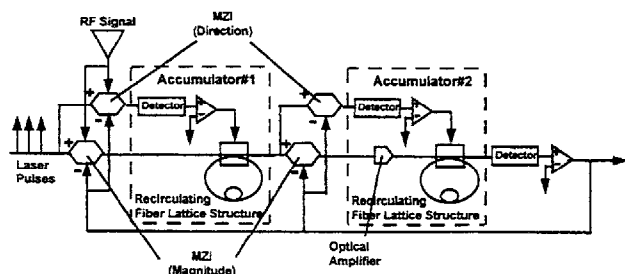
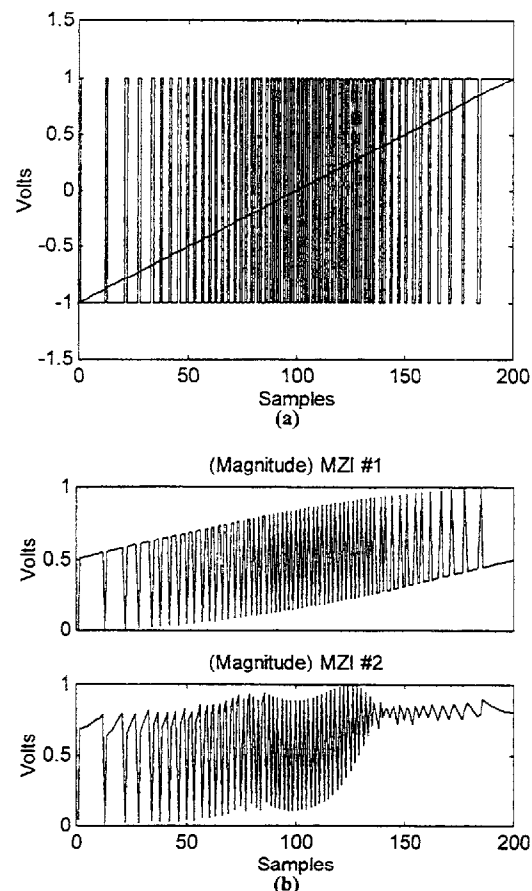
The quantization utilized in $\Sigma\Delta M$ introduces noise in the modulator. The quantization error e is treated as white noise having probability of lying anywhere in the range $\pm\Delta/2$, where Δ is the level spacing (normalized units) between quantized levels. Its mean-square value is given by¹

$$e_{\text{rms}}^2 = \frac{1}{\Delta} \int_{-\Delta/2}^{+\Delta/2} e^2 de = \frac{\Delta^2}{12}. \quad (12)$$

The oversampling ratio (OSR), defined as the ratio of the sampling frequency f_s to the Nyquist rate $2f_0$, is given by the integer

$$\text{OSR} = \frac{f_s}{2f_0} = \frac{1}{2f_0\tau}. \quad (13)$$

The noise power in the signal band can be shown to be


 Fig. 12 Block diagram of second-order electro-optic $\Sigma\Delta M$.

 Fig. 13 Transfer characteristic of a second-order electro-optic $\Sigma\Delta M$: (a) 200 input sampled-data values versus the output and (b) outputs at first and second accumulator stages.

$$n_0^2 = \int_0^{f_0} e^2(f) df = e_{\text{rms}}^2 (2f_0\tau) = \frac{e_{\text{rms}}^2}{\text{OSR}}. \quad (14)$$

It is evident that oversampling reduces the in-band root-mean-square (rms) quantization noise n_0 by the square root of the OSR.

The feedback loops in the $\Sigma\Delta M$ help shape the spectrum of the modulation noise by moving most of the noise outside the signal band. The filters used in the loops reduce the net noise in the signal band. The $\Sigma\Delta M$ subtracts the previous value of the quantization error from the present error. In the case of two feedback loops, the modulation noise becomes the second difference of the quantization error. The SNR for a second-order $\Sigma\Delta M$ can be predicted from¹

$$\frac{n_0}{\Delta} = \frac{\pi^2}{\sqrt{60}} (\text{OSR})^{-5/2}. \quad (15)$$

For a second-order $\Sigma\Delta M$, the SNR increases at 15 dB/octave and 6 dB/bit. Thus for OSR=128 and $\Delta=2$, and

$n_0 = -97$ dB. For a signal strength of 1 (i.e., 0 dB), $\text{SNR} = -n_0 = 97$ dB. At 6 dB/bit, this translates to 16 bits of resolution.

5 16-Bit Second-Order Example

In this section, the design of a 16-bit, $f_0 = 1$ MHz, second-order device is detailed. There are three fundamental limitations associated with digitizing wideband signals: sample time fluctuation, interaction time (laser pulse width), and thermal noise. These limitations limit the bit resolution B of the A to D process. It has been shown, in terms of the bit resolution and the maximum frequency to be digitized, that the jitter δt satisfies¹¹

$$\delta t < \frac{1}{2^{B+1} \pi f_{\max}} \quad (16)$$

Similarly, the pulse width, Δt satisfies

$$\Delta t < \frac{(3/2^{B-1})^{1/2}}{\pi f_{\max}} \quad (17)$$

For the condition that sampling is performed at the Nyquist rate, i.e., $f_{\text{SN}} = 2 f_{\max}$, the corresponding effects on the bit resolution, from Eq. (16), is

$$B = \frac{\log_{10}[2/(\pi f_{\text{SN}} \delta t)]}{\log_{10}(2)} - 1 \quad (18)$$

and from Eq. (17),

$$B = \frac{\log_{10}[\sqrt{12}/(\Delta t \pi f_{\text{SN}})]^2}{\log_{10}(2)} + 1 \quad (19)$$

Equations (18) and (19) are shown plotted versus the Nyquist sampling frequency in Fig. 14 for $\delta t = 2.4$ ps, $\Delta t = 3$ ns and $\delta t = 0.2$ ps, $\Delta t = 100$ ps. These values correspond to our 16-bit example, and the capabilities of today's commercial off-the-shelf mode-locked lasers, respectively.

To demonstrate the limitation created by thermal noise, a thermal noise power¹²

$$P_n = 4kTf_{\max} \quad (20)$$

is assumed. The ratio of signal power across a reference resistor R to noise power can then be evaluated according to

$$\left(\frac{S}{N}\right)_{\text{dB}} = 10 \log \frac{\langle V^2 \rangle}{R P_n} \quad (21)$$

After taking a reference voltage with unity rms and a reference load resistance of $R = 50 \Omega$, it follows after letting¹³

$$\left(\frac{S}{N}\right)_{\text{dB}} = 6B + 2 \quad (22)$$

that

$$B = \frac{1}{6} \left[10 \log \left(\frac{1}{100kTf_{\text{SN}}} \right) - 2 \right], \quad (23)$$

where again we have taken $f_{\max} = f_{\text{SN}}/2$. For purposes of comparison, Eq. (23) is also plotted in Fig. 14. For any given system, the bit resolution is limited by the effect (thermal, jitter, interaction time) that has the lowest value in Fig. 14. For our example, a 1-MHz signal having a Nyquist rate of 2 MHz can be digitized with 16 bits of resolution as long as the jitter ≤ 2.4 ps, and the pulse width is ≤ 3 ns. Since the guidelines, Eqs. (16) and (17), are fundamentally only dependent on the bandwidth (BW) of the signal being sampled, the jitter and interaction time limitations can be extracted from Fig. 14 for the $\Sigma-\Delta$ design.

For second-order $\Sigma-\Delta$ designs it is well known that the OSR must satisfy

$$\text{OSR} = \left[\frac{\sqrt{15}}{\pi^2} 10^{-(6B+2)/20} \right]^{-0.4} \quad (24)$$

For $B = 16$, an oversampling ratio of 132 results. Therefore, the pulses from the sampling laser must have a pulse repetition frequency of $f_s = 264$ MHz. The other significant specifications are obtained from Fig. 14. Note that these requirements are well within the capabilities of commercial off-the-shelf lasers.

A further consideration in the coherent fiber lattice structure is the round trip delay time τ of the recirculating lines. Since the constructive/destructive interference (integrate up/integrate down) depends on combining pulses in phase or out of phase, the length of fiber is important. For the 16-bit example, $\tau = 1/f_s = 3.8$ ns. In terms of the index of refraction of the single mode fiber n and the speed of light c , the delay time is $\tau = L(n/c)$ (Ref. 14). With $n = 1.48$, the required length of fiber for a 3.8 ns delay is $L = 0.77$ m.

To compensate for the lattice filter coefficient $C = 0.122$, an erbium-doped fiber amplifier (EDFA) with a gain of 15 is used. This gain value is in the linear region of the EDFA gain versus pump power characteristics (amplifier pumping efficiency), which permit changing the power gain by electronic means.¹⁵

6 Conclusions

The $\Sigma\Delta$ oversampling A/D modulator architecture uses limit cycles in quantized feedback loops to provide an accurate digital representation of the input signal. The second-order $\Sigma\Delta M$ provides a stable and robust design that is highly tolerant of circuit imperfections and component mismatch. The major limitations of this method are fast cycle times and bandwidth. The use of fiber optic technology eliminates these limitations. An integrated optical second-order $\Sigma\Delta$ architecture allows the processing of wideband rf signals. The integrated optical $\Sigma\Delta M$ design presented in this paper is a fairly straightforward extension of the electronic design using standard integrated optical devices. Current simulation results confirm design feasibility.

Future efforts include further optimization of the current integrated optical design. Modifications may include the possibility of optimizing the magnitude and direction of each accumulation stage using only one interferometer. The

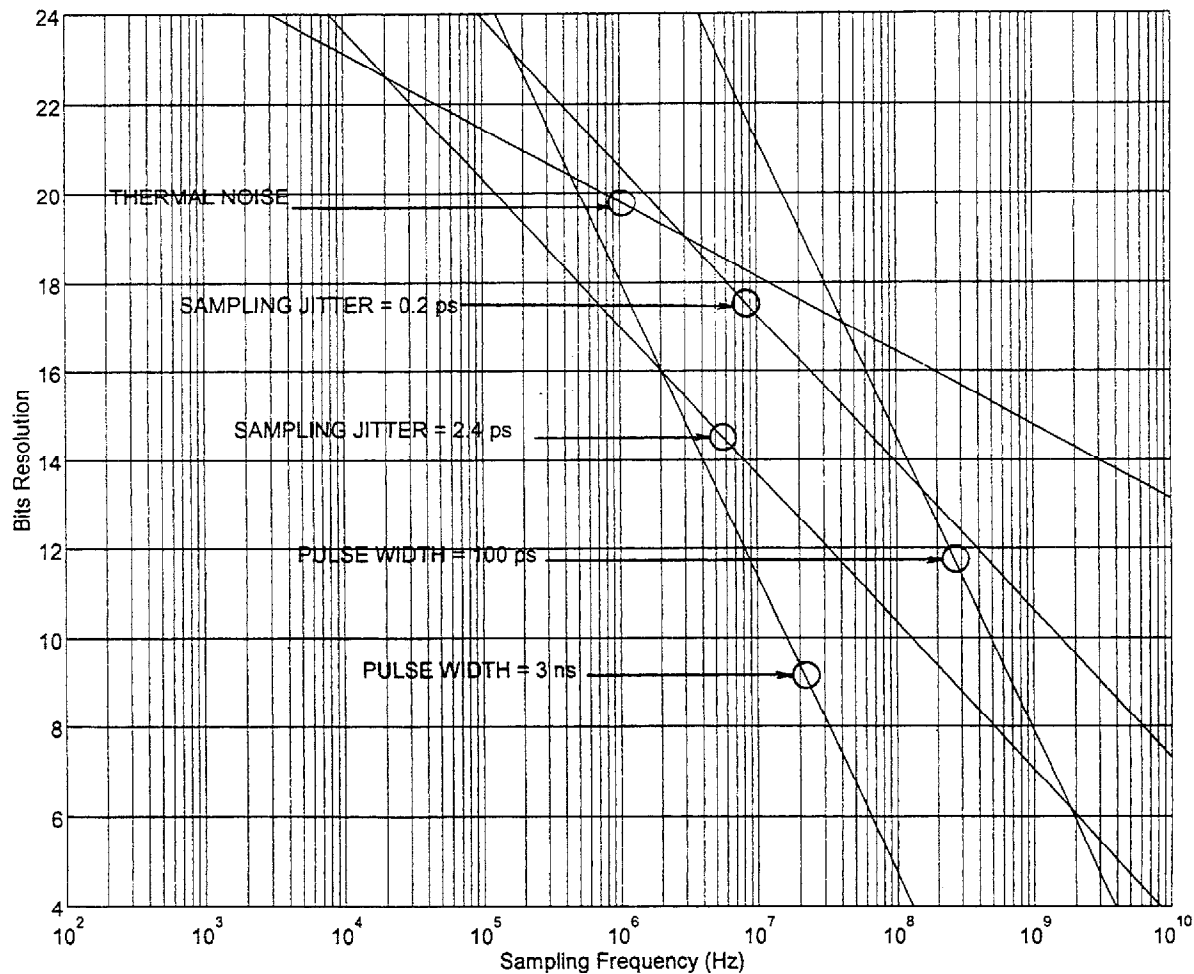


Fig. 14 Fundamental limitations in sampling wideband signals.

accumulation stages of the integrated optical $\Sigma\Delta M$ are modeled by fiber lattice structures with similar system transfer functions. More rigorous modeling of these delay line structures and analysis of the optical amplifiers are needed for future hardware implementation. Since the output of the modulator represents the input signal together with modulation noise, there is still a need to decimate the modulated signal. A multistage decimation is needed to lower the word rate and remove high-frequency modulation noise before the signal is resampled at the Nyquist rate. Design issues to be studied include nonlinearities associated with interferometers, stability of the accumulator stages, effects of net gains in the feedback loops, and the effects of modulation noise and oversampling frequency (OSR) on bit resolution.

Acknowledgments

This work was supported by the Space and Naval Warfare Systems Command. The authors would like to thank the reviewers for their helpful comments. Also, thanks to Mr. Jim Allen who typeset the manuscript.

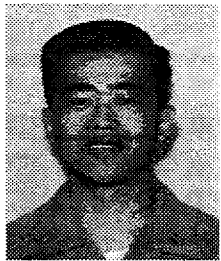
References

1. J. C. Candy and G. C. Temes, "Oversampling methods for A/D and D/A conversion," in *Oversampling Delta-Sigma Data Converters*, J. C. Candy and G. C. Temes, Eds., pp. 1-29, IEEE Press, New York (1992).
2. J. C. Candy, "A use of limit cycle oscillations to obtain robust analog-to-digital converters," *IEEE Trans. Commun.* **COM-22**, 298-305 (Mar. 1974).
3. C. C. Cutler, "Transmission systems employing quantization," U.S. Patent No. 2,927,962 (1960).
4. B. E. Boser and B. A. Wooley, "The design of sigma-delta modulation analog-to-digital converters," *IEEE J. Solid State Circ.* **23**(6), 1298-1308 (1988).
5. B. L. Shoop and J. W. Goodman, "Optical oversampled analog-to-digital conversion," *Appl. Opt.* **31**(26), 5654-5660 (1992).
6. B. L. Shoop and J. W. Goodman, "A first-order error diffusion modulator for optical oversampled A/D conversion," *Opt. Commun.* **93**, 167-172 (1993).
7. B. L. Shoop, "Second-order cascaded optical error diffusion modulators for oversampled analog-to-digital converters," *Opt. Commun.* **102**, 125-132 (1993).
8. R. C. Alfiness, "Waveguide electro-optic modulators," *IEEE Trans. Microwave Theory Tech.* **MTT-30**(8), 1121-1137 (1982).
9. P. E. Pace, S. J. Ying, J. P. Powers, and R. J. Pieper, "Optical SD analog-to-digital converters for high-resolution digitization of antenna signals," in *Proc. PSAA-V 5th Ann. ARPA Symp. on Photonic Systems for Antenna Applications*, pp. 412-416 (Jan. 1995).
10. B. Moselehi, J. W. Goodman, M. Tur, and H. J. Shaw, "Fiber-optic lattice signal processing," *Proc. IEEE* **72**(7), 909-930 (1984).
11. P. E. Pace and D. Styer, "High resolution encoding process for an

- integrated optical analog-to-digital converter," *Opt. Eng.* 33, 2638-2645 (1994).
12. A. Yariv, *Optical Electronics*, 3rd ed., Holt Rinehart and Winston, New York (1985).
13. R. Freeman, *Telecommunications Transmission Handbook*, Wiley Interscience Publications, John Wiley & Sons, New York (1991).
14. J. P. Powers, *An Introduction to Fiber Optic Systems*, Aksen Associates, Inc., Boston, MA (1993).
15. J. Capmany and J. Cascon, "Direct form I fiber-optic discrete time signal processors using optical amplifiers and embedded Mach-Zehnder structures," *IEEE Photonic Technol. Lett.* 5, 842-844 (1993).



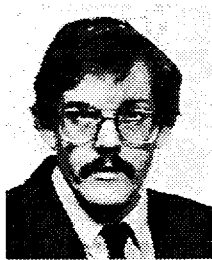
Phillip E. Pace is an associate professor in the Department of Electrical and Computer Engineering at the Naval Postgraduate School (NPS). He received BS and MS degrees from the Ohio University in 1983 and 1986, respectively, and a PhD from the University of Cincinnati in 1990, all in electrical and computer engineering. Dr. Pace has been a principal investigator on numerous research projects in the areas of optical signal processing and electronic warfare systems. He currently directs the Center for Joint Services Electronic Warfare at NPS and recently received the 1995 AOC award for Academic Training. Dr. Pace is a member of SPIE, IEEE, and the AOC.



Stephen J. Ying is a lieutenant in the United States Navy. He received his BS degree in computer science from Stanford University in 1990 and an MS degree in electrical and computer engineering from the Naval Postgraduate School in 1995. His research interests include optical signal processing and electronic warfare systems.



John P. Powers is the dean of engineering and computational science and a professor of electrical and computer engineering at the Naval Postgraduate School. He received the BS degree (summa cum laude) from Tufts University in 1965, an MS degree from Stanford University in 1966, and a PhD from the University of California, Santa Barbara, in 1970, all in electrical engineering. His current research interests are in acoustical imaging, acousto-optic signal processing, fiber optic communications, and other electro-optic applications. He is the author of the text, *Introduction to Fiber Optic Systems*. Dr. Powers is a member of IEEE, ASA, and OSA.



Ronald J. Pieper is an associate professor in electrical engineering at the Naval Postgraduate School. He received a BS degree in physics from the University of Missouri, St. Louis, in 1974, an MS degree in physics and an MSEE degree from the University of Wisconsin, Madison, in 1976 and 1979, respectively, and a PhD in electrical and computer engineering from the University of Iowa, Iowa City, in 1984. Dr. Pieper is a member of SPIE and OSA, a senior member of IEEE, and a registered professional engineer in Virginia. His research interests include acousto-optics and image processing.